Journal of MATERIALS RESEARCH

Article
DOI:10.1557/s43578-023-01041-6

Calibration and data-analysis routines for nanoindentation with spherical tips

Diana Avadanii[1,a], Anna Kareer[2], Lars Hansen[3], Angus Wilkinson[2]

[1] Department of Earth Sciences, University of Oxford, Oxford, UK
[2] Department of Materials, University of Oxford, Oxford, UK
[3] Department of Earth and Environmental Sciences, University of Minnesota, Minneapolis, USA
[a] Address all correspondence to this author. e-mail: diana.avadanii@univ.ox.ac.uk

Received: 5 February 2023; accepted: 9 May 2023

Instrumented spherical nanoindentation with a continuous stiffness measurement has gained increased popularity in microphysical investigations of grain boundaries, twins, dislocation densities, ion-induced damage, and more. These studies rely on different methodologies for instrument and tip calibration. Here, we test, integrate, and re-adapt published strategies for tip and machine-stiffness calibration for spherical tips. We propose a routine for independently calibrating the effective tip radius and the machine stiffness using standard reference materials, which requires the parametrization of the effective radius as a function of load. We validate our proposed workflow against key benchmarks and apply the resulting calibrations to data collected in materials with varying ductility to extract indentation stress–strain curves. We also test the impact of the machine stiffness on recently proposed methods for identification of yield stress. Finally, we synthesize these analyses in a single workflow for use in future studies aiming to extract and process data from spherical nanoindentation.

Introduction

Instrumented nanoindentation has become a widely–used technique for material characterization. The array of available tip geometries allows material analysis over a wide range of stress states. Indentation with a rigid, spherical tip has recently gained popularity due to key advantages of this geometry compared to sharp tip geometries (e.g., Berkovich). Indentation with a sphere induces a stress field under the indenter that is not self similar, and therefore, the indentation strain progressively increases with indentation depth [see Chapter 3 in 1–4]. Thus, load–displacement data can be transformed into indentation stress–strain curves, which facilitate the investigation of the full elasto-plastic response of materials [for review, see 3]. Moreover, nanoindentation with indenters of varying radii provides insight into size effects associated with deformation and enables correlation of small-scale material testing with macroscopic tests [e.g., 3]. For example, in certain materials, indentation using tips with large radii results in stress–strain curves with a hardening coefficient similar to that of uniaxial tests, while data obtained using indenters with smaller radii display an indentation size effect [e.g., 5, 6]. In spherical nanoindentation, the indentation size effect is underpinned by both material hardening with increasing indentation strain, as well an increase in hardness with decreasing spherical radii [2, 5, 7–9]. Finally, bursts of displacement in the stress–strain curves (called 'pop-ins') provide valuable insight into initiation of plasticity at small scales and display an additional size effect in spherical nanoindentation, in which the stress at pop-in increases with decreasing tip radius [10–13].

The potential to produce a large number of measurements and generate indentation stress–strain curves from a small volume of material makes spherical nanoindentation a desirable technique with a wide range of applications. For example, spherical nanoindentation has been deployed to investigate yield stress and size effects in brittle engineering ceramics and natural minerals [e.g., 10, 14–18], the mechanical properties of twin and grain boundaries in metals [e.g., 19–21], the effects of ion-induced damage in metals and alloys [e.g., 22–24], the relationship between structure and mechanical properties in biomaterials (bone [e.g., 25], human enamel [e.g., 26]), elasto-plastic transitions in bulk metallic glasses [e.g., 27, 28], and fracture in thin films [e.g., 29, 30]. This versatility of mechanical testing using

© The Author(s) 2023

spherical indentation has motivated studies on the reliability of measurements and prompted efforts to improve data analysis. Investigations into the methodology of spherical indentation highlight the importance of accurate knowledge of tip radius [31–33], machine stiffness, [32, 34, 35], differences among nanoindenter apparatus [35], and the impact of different data-analysis routines on the extracted material properties [3, 36].

In this contribution, we test, integrate, and adapt several published strategies for calibration of spherical tip shape and machine stiffness, and implement a routine to calibrate the effective radius and machine stiffness using purely elastic indentation data collected on materials with varying elastic moduli. This synthesis results in an improved workflow to accurately extract stress–strain curves. We also develop a procedure for characterization of the effective tip shape and machine stiffness for tips that are not perfectly spherical, relying on the obtained indentation data from reference materials. We emphasize that the cumulative impact of imperfections in spherical tips, inconsistencies in sample mounting, and variations among instruments reduce the repeatability and overall meaningful interpretation of data collected across multiple studies. To this end, we outline a calibration routine using fused silica, sapphire, and glassy carbon as reference materials. We then implement the resulting calibration to extract indentation stress–strain curves from tungsten, olivine, and titanium. Details of the experiment set-up are outlined in the "Experimental aspects" section. We suggest that future studies using spherical nanoindentation would benefit from detailed reports of how the tip and machine-stiffness calibration satisfy different benchmarks for meaningful comparison among published results. Ultimately, we intend for this contribution to serve as a detailed guide to deliver the full potential of spherical nanoindentation as a materials characterization technique with application to a broad range of materials with varying ductility.

Results and analysis

Theoretical background

Instrumented nanoindentation measures the displacement of the indenter tip in response to an applied load, P. The total measured displacement, h_{total}, is a combination of the displacement due to surface deformation of the sample, h_{sample}, and the deflection due to the machine stiffness, h_{mach} (Fig. A.1, Supplementary Materials). This interaction can be expressed as two deforming elements connected in series, for which the displacements are [37–39]

$$h_{\text{total}} = h_{\text{sample}} + h_{\text{mach}} \tag{1}$$

The value of h_{mach} can be estimated from the machine stiffness, S_{mach}, according to $h_{\text{mach}} = P/S_{\text{mach}}$, where the machine stiffness accounts for the combined stiffness from the indenter tip and the loading frame. The common procedure is to determine S_{mach} for an instrument by performing a series of experiments with a Berkovich tip in a material with known elastic modulus. This method allows both the area function describing the tip and the machine stiffness to be determined simultaneously [e.g., 38]. The obtained value of the machine stiffness is used as the default stiffness, S_{default}, which is generally applied by the instrument software when collecting and reporting new data. However, previous studies using spherical indenters have indicated that the stiffness during experiments is a function of the applied load, rather than a single value [35, 37]. Consequently, this procedure for calibration of the area function and machine stiffness can lead to systematic errors in subsequent experiments if the applied loads are significantly different than those used in the calibration [32].

It is possible to explicitly implement a calibration routine for spherical indentation tips in order to identify S_{mach} for each machine-tip pair, as well as to determine the effective radius of the tip. Following Li and Bhushan [37], we express the reported displacement as follows:

$$h_{\text{rep}} = h_{\text{total}} - \frac{P}{S_{\text{default}}} + h_0, \tag{2}$$

where h_0 accounts for errors arising from the initial contact between the sample surface and the indenter tip (Fig. A.1).

Because the stiffness of a particular indenter tip combined with the stiffness of the other components of the instrument are unknown, we use Eqs. 1 and 2 to describe h_{rep} as follows:

$$h_{\text{rep}} = h_{\text{sample}} + \frac{P}{S_{\text{mach}}} - \frac{P}{S_{\text{default}}} + h_0. \tag{3}$$

For cases in which the response of the material is purely elastic, h_{sample} can be modeled according to Hertzian mechanics as the elastic displacement, h_e [4],

$$h_e = P^{2/3}\left(\frac{4}{3}\sqrt{R_{\text{eff}}}E_{\text{eff}}\right)^{-2/3}, \tag{4}$$

for which

$$\frac{1}{E_{\text{eff}}} = \frac{1-\upsilon_s^2}{E_s} + \frac{1-\upsilon_i^2}{E_i} \tag{5}$$

and

$$\frac{1}{R_{\text{eff}}} = \frac{1}{R_s} + \frac{1}{R_i}. \tag{6}$$

E_{eff} and R_{eff} are the reduced elastic modulus and tip radius and are expressed as a function of the elastic moduli and Poisson's ratios of the sample (E_s and υ_s) and indenter tip (E_i and υ_i) and of the radius of the sample surface (R_s) and indenter tip (R_i). For a purely elastic contact and a flat sample surface, the curvature of the surface is infinity so that $R_{\text{eff}} = R_i$ (Fig. A.1).

© The Author(s) 2023

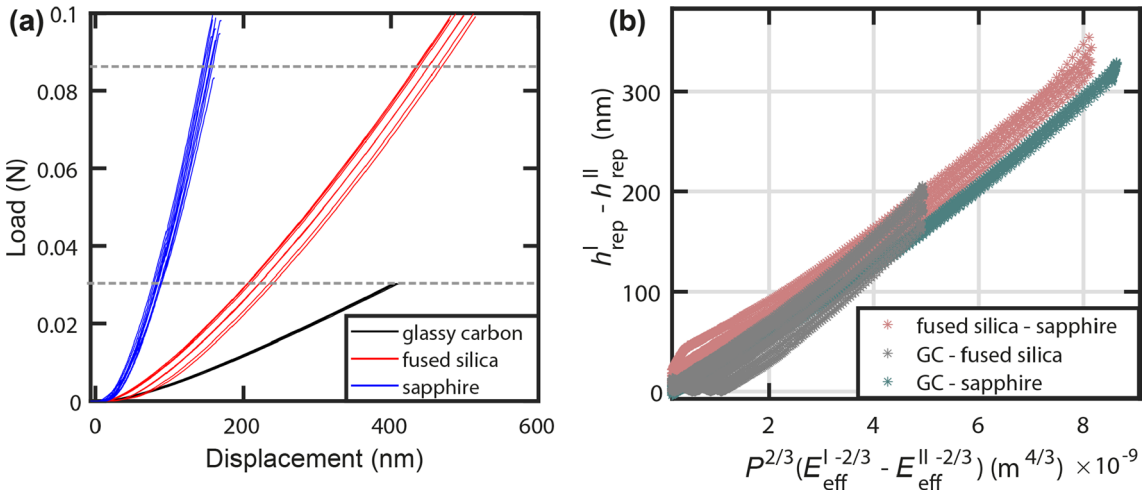

Figure 1: (a) Load–displacement data collected with a spherical tip with a nominal radius of 10 μm in different materials with known moduli. (b) Difference between measured displacements in two materials at similar load. The end cut-off load for each set of experiments is marked by the dashed horizontal lines in (a). The slope of these curves is proportional to the effective tip radius according to Eq. 8.

Calibrations on materials with known moduli

Determination of effective radius

Studies employing spherical nanoindentation implement various strategies for calculating the effective radius, R_{eff} [3, 31, 33, 37]. The value of R_{eff} can be calculated by using Eq. 6 and the nominal tip radius provided by the manufacturer [14]. More commonly, R_{eff} is calculated by fitting Eq. 4 to data collected in fused silica [3, 13, 39]. Alternatively, using data from fully elastic experiments in materials with a wide range of elastic moduli, optimum values of R_{eff} can be simultaneously determined alongside other variables (e.g., machine stiffness) with the constraint that R_{eff} is as constant with depth as possible [e.g., 10, 33, 40]. Complications in implementing these methods arise due to the impact of machine stiffness on reported displacement values and of tip shape imperfections, which are difficult effects to deconvolve. These errors can lead to unrealistic differences in the values of R_{eff} obtained with different reference materials (e.g., fused silica and sapphire) [10, 33, 37]. Moreover, errors in the calibration of R_{eff} can lead to inconsistencies in stress–strain measurements on the same material with different indenter tips. These potential discrepancies motivate the need for a calibration routine in which the machine stiffness and effective radius are both determined in a self-consistent manner [37].

To circumvent these issues, we implement the method proposed by Li et al. [32] to find the machine stiffness and effective radius for each machine-tip pair in Table 1. Although Li et al. [32] applied their calibration routine to two reference materials, we extend this analysis to three reference materials. This approach relies on the difference in reported displacements at the same load in elastic experiments on different materials with known elastic moduli. Following Li et al. [32], we rearrange Eq. 3 to define the error in displacement, h_{err}, as follows:

$$h_{err} = h_{rep} - h_e - h_0 = \frac{(S_{default} - S_{mach})P}{S_{default}S_{mach}}. \quad (7)$$

TABLE 1: Summary of experiments. Note that the experiments in the reference materials with known elastic moduli are experiments in the elastic deformation regime only.

Material	Nominal tip radius, R_n					Young's Modulus, E_s, (GPa)	Poisson ratio, ν_s	Grain size (μm)
	2 μm	5 μm	10 μm	20 μm	50 μm			
	Maximum load (N)							
Fused silica	$2.5 * 10^{-3}$	$8 * 10^{-2}$	$1 * 10^{-1}$	$2 * 10^{-1}$	$3 * 10^{-1}$	72	0.17	Single crystal
Sapphire	$2.5 * 10^{-3}$	$8 * 10^{-2}$	$1 * 10^{-1}$	$2 * 10^{-1}$	$3 * 10^{-1}$	420	0.28	Single crystal
Glassy carbon	$1.5 * 10^{-3}$	$1 * 10^{-2}$	$3 * 10^{-2}$	$5 * 10^{-2}$	$1 * 10^{-1}$	34	0.27	–
Olivine	$8 * 10^{-2}$	$2.5 * 10^{-1}$	$3.8 * 10^{-1}$	$6.5 * 10^{-1}$	$6.5 * 10^{-1}$	–	0.24	Single crystal
Ti	$2.5 * 10^{-2}$	$8 * 10^{-2}$	$1.5 * 10^{-1}$	$3 * 10^{-1}$	$4 * 10^{-1}$	–	0.35	35
W	$5.5 * 10^{-2}$	$2 * 10^{-2}$	$3.2 * 10^{-1}$	$6 * 10^{-1}$	$6 * 10^{-1}$	–	0.29	> 50

© The Author(s) 2023

The main assumption with this approach is that, at a given load, h_{err} is the same for different reference materials. For two reference materials (noted as I and II), using Eq. 3 and data collected at the same load, we can subtract the reported elastic displacement in material II, h^{II}_{rep}, from the reported elastic displacement in material I, h^{I}_{rep}. The $\frac{P}{S_{mach}}$ and $\frac{P}{S_{default}}$ terms in Eq. 3 corresponding to each material cancel out for the same load P such that [32]

$$h^{I}_{rep} - h^{II}_{rep} = P^{2/3}\left(\frac{4}{3}\sqrt{R_{eff}}\right)^{-2/3}\left(E^{I}_{eff}{}^{-2/3} - E^{II}_{eff}{}^{-2/3}\right) + h^{I}_{0} - h^{II}_{0}. \quad (8)$$

We apply Eq. 8 to data collected from fused silica, glassy carbon, and sapphire as outlined in the "Experimental aspects" section. In Fig. 1, we display the reported elastic load–displacement curves in the reference materials collected with a tip with nominal radius $R_n = 10\ \mu m$, and mark the load and displacement used in Eq. 8 with a dashed horizontal line. Figure 1(b) reports the differences calculated using Eq. 8 between reported displacement in fused silica and sapphire, glassy carbon and fused silica, and glassy carbon and sapphire as a function of a term proportional to $P^{2/3}$. Thus, according to Eq. 8, the slope of the graph in Fig. 1(b) is proportional to R_{eff}, and the intersection with the vertical axis is the difference in the displacement error due to surface contact in the two materials ($h^{I}_{0} - h^{II}_{0}$).

One key observation in Fig. 1(b) is that the average slope of the curves systematically varies among the three pairs of reference materials. This observation is ubiquitous among our experiments, as can be seen in Fig. 2 and Table A.1 (Supplementary Materials), which demonstrates that the best-fit R_{eff} varies by up to 40% depending on the pair of reference materials. This result is contrary to expectations arising from the analysis of Li et al. [32], which suggests that R_{eff} should not depend on the reference materials used in calibration.

Part of this discrepancy results from the curves in Fig. 1(b) departing from linearity, which implies that R_{eff} is not a constant for any given calibration. This issue is accentuated in Fig. 3(a), which presents data comparing fused silica to sapphire and a linear fit assuming constant R_{eff}. There is clearly curvature in the data not captured by the linear fit. Since the subtraction method proposed by Li et al. [32] accounts for the effects of machine stiffness when calculating R_{eff}, we interpret the curvature of the data in Fig. 3(a) to instead result from departure of the tip shape from a perfect sphere. Imperfections in tip shape could be accounted for by the parametrization of R_{eff} as a function of displacement. However, measured displacements are also affected by the machine stiffness, which is unknown at this point in the analysis. Therefore, we instead choose to

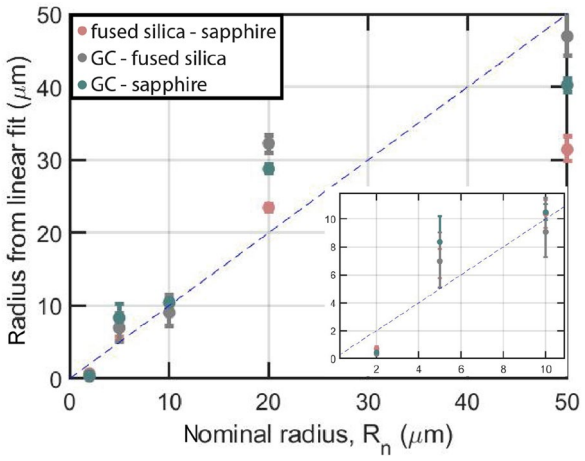

Figure 2: Summary of results for effective radius determined as the slope of a line fit through data calculated as the subtraction of elastic load–displacement curves at the same load in different reference materials following the method of Li et al. [32] (Eq. 8). The dashed line represents the 1:1 proportionality. The values can be found in Table A.1 (Supplementary Materials).

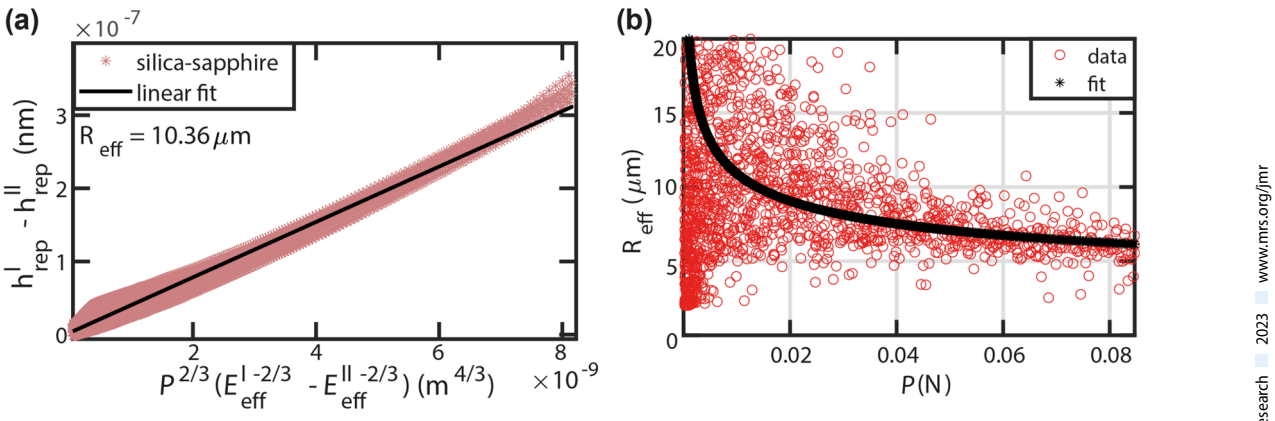

Figure 3: (a) Linear fit for a spherical tip with a nominal radius of 10 μm following Li et al. [32]. Note the curvature in the data obtained by subtracting sapphire displacement from fused silica displacement according to Eq. 8. (b) Effective radius calculated using the first numerical derivative of data in (a) against load and an exponential fit. All values for R_{eff} in Fig. 2 and the values for R_{eff} at a constant load can be found in Supplementary Materials, Table A.1.

© The Author(s) 2023

express the effective radius as a function of load. Figure 3(b) presents R_{eff} as a function of load as calculated from the first derivative of the curve in Fig. 3(a). We fit an offset power law function (i.e., $f(x) = \mathrm{a}x^{\mathrm{b}} + \mathrm{c}$) to these data to allow R_{eff} to be easily estimated for any given load. This function captures the values of effective radius with load at the middle and end segments of the indentation data. We only fit this function to data comparing fused silica and sapphire because the data involving glassy carbon correspond to smaller loads [Fig. 1(a)], for which the data are considerably noisier, as demonstrated in Fig. A.2 (Supplementary Materials). The trend in Fig. 3(b) matches the expectation of convergence to a single value for R_{eff} at larger loads. Comparing Figs. 2 with 3(b), we note that at higher loads, the calculations following Li et al. [32] overestimate the values for R_{eff}, which could lead to underestimations of stress [e.g., 41, 42] (see Table A.1).

Determination of machine stiffness

For a robust interpretation of stress–strain curves obtained using spherical indentation, the impact of machine stiffness has to be determined for each combination of instrument and tip and can be reported as a function of load [32, 34, 35]. To assess the magnitude of the machine stiffness, Fig. 4(a) compares the reported loads and displacements to the predicted elastic displacement using Eq. 4. In this equation, we implement R_{eff} either as a constant [blue symbols, similar to Fig. 3(a)] or as a function of load [red symbols, similar to Figs. 3(b), A.2]. Although using the load-dependent R_{eff} in Fig. 4(a) results in better agreement with the reported data, there is still some mismatch in the displacements, which corresponds to h_{err} and which we attribute to the stiffness of the machine-tip pair. We use R_{eff} as a function of load in conjunction with h_{err} and the known value of S_{default}, provided by the manufacturer and stated in "Experimental aspects" section, to calculate S_{mach} according to Eq. 7. Rearranging to Equation 7, indicates that S_{mach} has large values if h_{err} has values close to the displacement error given by P/S_{default}. We plot this machine stiffness, S_{mach}, as a function of load for sapphire and fused silica in Fig. 4(b and c). For comparison, we also plot S_{mach} assuming R_{eff} is constant (values from Table A.1. column 1). In Fig. 4(b and c), we plot the result of calculations of S_{mach} among tests in sapphire and fused silica, as there is no particular reason for using one data set over another when substituting in Eq. 7. We emphasize that the values of S_{mach} calculated with for sapphire and fused silica both converge to $\sim 0.7 * 10^7$ N/m for a tip with a nominal radius of 20 μm (Fig. 4). Note that the variability in S_{mach} resulting from tests on sapphire (Fig. 4b) and fused silica [Fig. 4(c)] is directly related to how well the Hertzian prediction in Fig. 4(a) fits the reported data. As demonstrated in Fig. 4(a), the elastic prediction overestimates the reported displacement, which means $h_{\text{rep}} - h_{\text{e}}$ is negative, and therefore, the resulting effective machine-tip stiffness

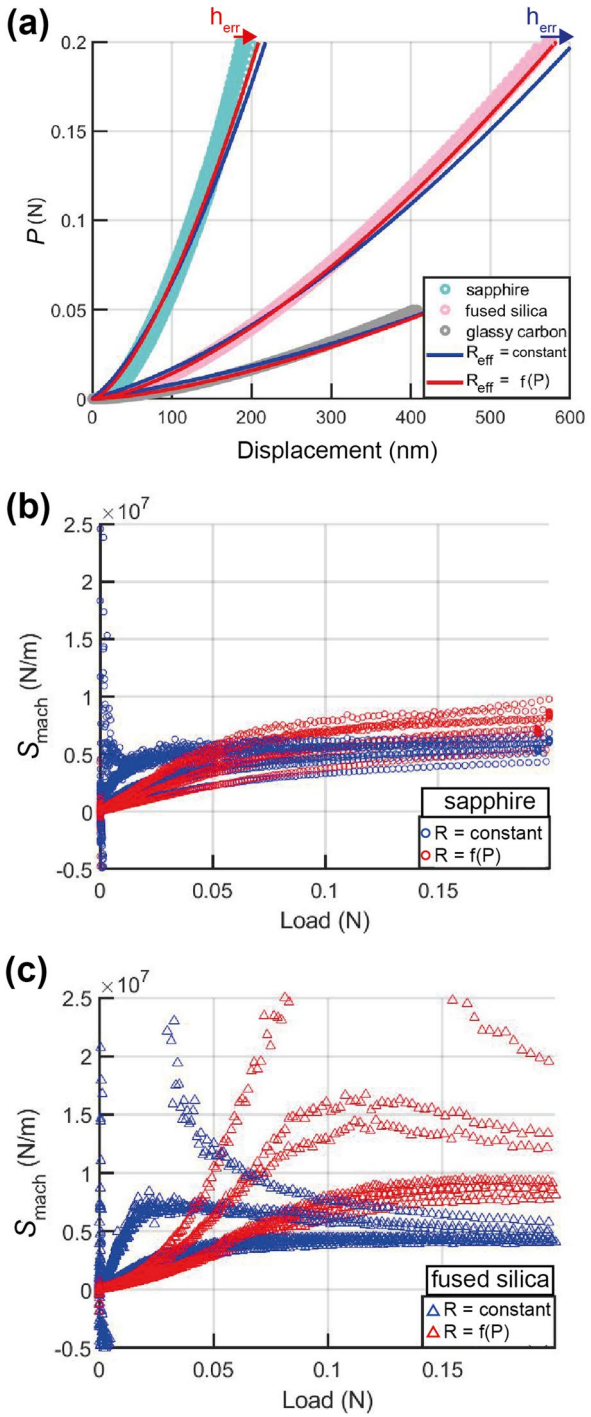

Figure 4: (a) Load–displacement data for a spherical tip with a nominal radius of 20 μm in different materials with known moduli overlapped with predictions using a constant effective radius (blue) and radius as a function of depth (red) in Eq. 4. The arrows are proportional to h_{err} at the maximum load, as defined in Eq. 7. (b) Calculations of machine stiffness using sapphire data in Eq. 7. (c) Calculations of machine stiffness using fused silica data in Eq. 7.

$(P/(h_{\text{rep}} - h_{\text{e}}))$ is negative (see Eq. 7). This effective negative effective machine-tip stiffness does not imply that the machine actually has negative stiffness. Instead, the negative effective stiffness

© The Author(s) 2023

results from the default stiffness used by the software, $S_{default}$, being smaller than the actual machine-tip stiffness (see Eq. 7).

The contribution of the stiffness of the machine-tip pair also needs to be accounted for when evaluating the reported harmonic contact stiffness. We model the machine-tip pair and the sample response as a series of elastic elements [37] and propose a correction for the reported harmonic contact stiffness using

$$\frac{1}{S_{corr}} = \frac{1}{S_{rep}} + \frac{1}{S_{default}} - \frac{1}{S_{mach}}, \tag{9}$$

where S_{corr} is the corrected contact stiffness and S_{rep} is the reported contact stiffness collected with $S_{default}$. We implement Eq. 9 with a variable S_{mach} by linearly fitting S_{mach} as a function of load in Fig. 4(b). We recognize that these data depart from linearity but implement a linear fit as a practical approximation in line with previous studies [e.g., 32]. In this step, choices regarding the range of data used in the fitting will impact the slope of the fitted line. This is the key step in which we recommend an iteration between the fitting procedure and the outcome of the data correction verified in the benchmarks presented in the next section.

Benchmarks

Calibrations of spherical tips can be assessed with a variety of key benchmarks. The most common benchmark in nanoindentation is observation of a constant Young's modulus with depth [e.g., 31, 43]. Following the derivation from Hackett et al. [14] and using Eqs. 4 and 9, we can express the effective Young's modulus as follows:

$$E^*_{eff} = \sqrt{\frac{S^3_{corr}}{6PR_{eff}}}. \tag{10}$$

Using Eq. 10, we assess the impact of different corrections and formulations for R_{eff} on the Young's modulus. Figure 5(a) demonstrates that using a constant effective radius (Table A.1., column 1) and the reported continuous stiffness measurement results in significant variability of the Young's modulus with depth. In contrast, Fig. 5(b) demonstrates that using a load-dependent R_{eff} [e.g., Fig. 3(b)] results in the convergence of E_{eff} towards expected values at relatively shallow depths.

Another important benchmark is a consistent effective tip shape measured in multiple reference materials over the elastic depth range. A plot of the contact depth, h_c, versus the contact radius, a, determined from the harmonic stiffness should essentially represent a profile of the effective indenter shape [3, 44] (Fig. A.1). In the case of elastic spherical indentation, the effective tip shape is expected to be the same during loading and unloading for a given tip regardless of which reference material is used. We calculate the contact depth (see Fig. A.1), h_c, using [3, 38, 45]

$$h_c = h_{rep} - \xi\frac{P}{S}, \tag{11}$$

where ξ is a geometric factor equal to 0.75 for spherical indents [1, 38]. Implementing corrections associated with the system stiffness, we calculate the corrected contact depth, h^*_c, as follows:

$$h^*_c = h_{rep} - h_{err} - \xi\frac{P}{S_{corr}}. \tag{12}$$

We calculate the contact radius using both reported and corrected values of the contact stiffness, [3, 38]

$$a = \frac{S_{rep}}{2E_{eff}} \tag{13}$$

and

$$a_{corr} = \frac{S_{corr}}{2E_{eff}}. \tag{14}$$

We compare the effective tip shape with the shape predicted for a perfect sphere with contact radius a_{pred} given by

$$a_{pred} = \sqrt{2R_i h_c - h_c^2}. \tag{15}$$

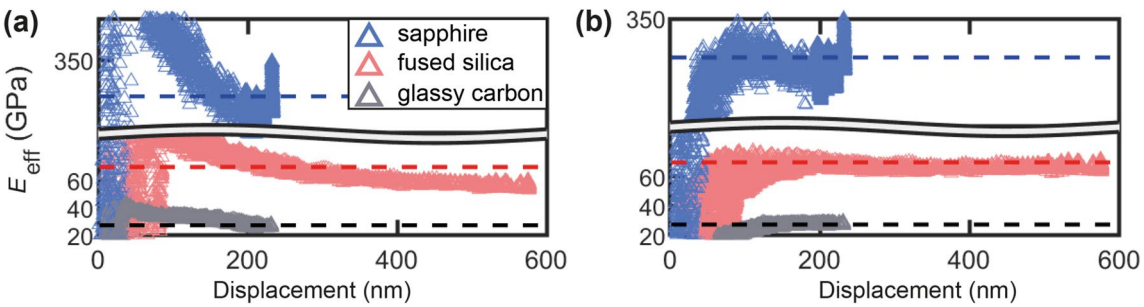

Figure 5: Comparison of Young's modulus calculated using Eq. 10 to expected values. Young's modulus is calculated using either (a) a constant effective radius (Table A.1, column 1) and reported values for the harmonic contact stiffness or (b) a load-dependent effective radius and contact stiffness corrected according to Eq. 9. Note the differences in vertical scales. The reference values of the effective Young's modulus are plotted with dashed lines and are calculated using the values in Table 1 and Eq. 5. These tests were conducted with a tip with nominal radius of R_n = 5 µm.

© The Author(s) 2023

Note that for perfectly elastic indents $h_c = h_e/2$ and $R_i = R_{eff}$ [3, 46].

Figure 6 summarizes the impact of the proposed calibration routines and data corrections on the effective tip shape. We observe in Fig. 6(a) that the uncorrected data display significant discrepancies between the apparent tip shape and the ideal predicted tip shape calculated using the constant radii summarized in Fig. 2 (Table A.1, column 1). We also observe that, the apparent tip shape varies depending on the reference material, with the sapphire dataset exhibiting the most significant discrepancies. Figure 6(b) indicates that our proposed strategies for data correction result in good agreement between the apparent tip shape and the tip shape calculated with the best-fit, constant radius in Eq. 15 and corrected data in Eq. 12. These corrections also result in a consistent apparent tip shape among different reference materials.

Characterization of materials with unknown Young's moduli

In "Calibrations on materials with known moduli" section we determined that two key parameters (the effective radius and machine stiffness) are needed for each combination of machine and indenter tip (Fig. 6) to calculate the Young's modulus and stress–strain curves using load–displacement data. In this section, we demonstrate how these calibrations may be implemented to extract stress–strain curves in samples with potentially unknown moduli, using W, Ti, and olivine as examples. The details of these experiments are described in "Experimental aspects" section (see Table 1).

Zero-point correction

A key step in analyzing reported load–displacement data is the identification of the point of zero-displacement and zero-load, i.e., the zero-point correction. The impact of the zero-point correction on the estimations of R_{eff} and stress–strain curves has been a focus in previous analyses of spherical nanoindentation data [3, 36, 47]. In our approach for calibrating spherical tips using reference materials of known elastic moduli, the last term in Eq. 8 already accounts for errors in the point of initial contact. However, the methods discussed above do not provide a means for finding the effective point of zero contact in data acquired in materials with unknown elastic moduli.

Kalidindi and Pathak [36] proposed a method for determining the effective point of contact by using the relationship

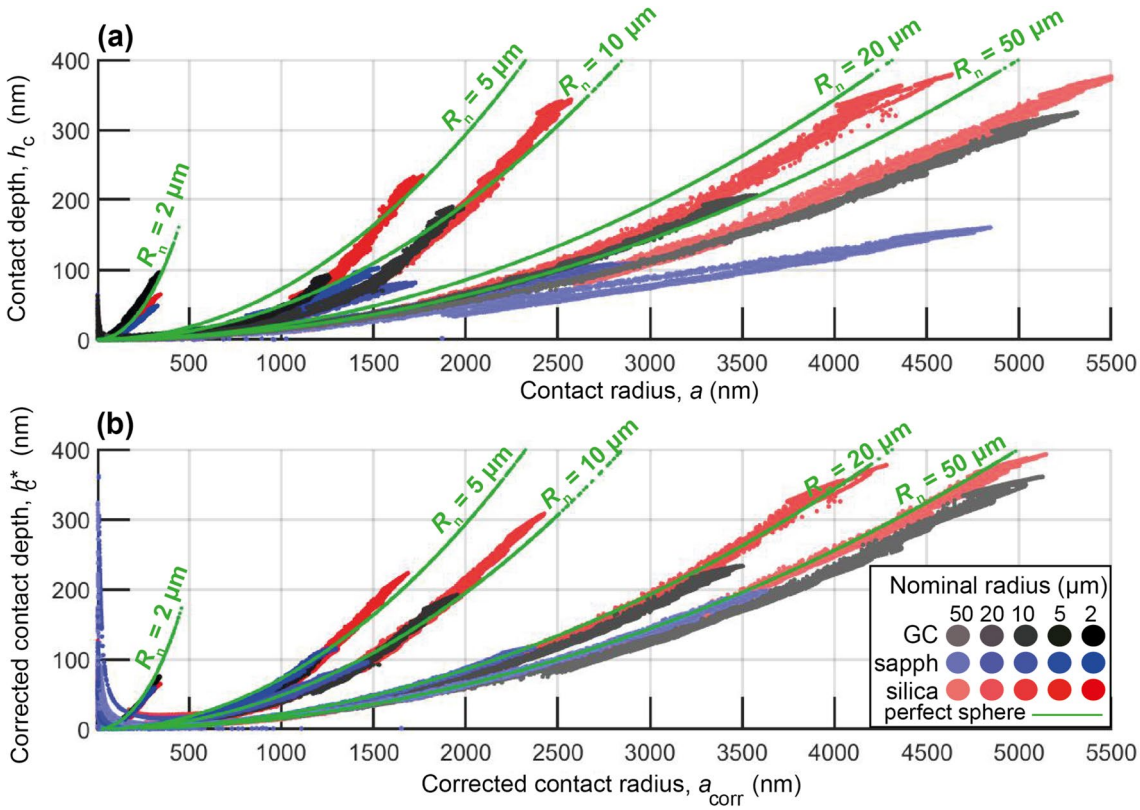

Figure 6: (a) The effective tip shape calculated with data as reported and (b) the effective tip shape calculated with corrected displacement and harmonic stiffness data for spherical tips with load-dependent radii. The green curve represents the tip shape for a perfect sphere with R_i values from Fig. 2 and presented in Table A.1 (column 1), and with the contact radius calculated using Eqs. 15 and 11 in panel (a), and Eqs. 15 and 12 in panel (b).

© The Author(s) 2023

between the reported load, displacement, and harmonic stiffness measurements for the elastic portion of an indentation test,

$$S_{\text{rep}} = \frac{3P}{2h_e} = \frac{3(P - P_0)}{2(h_e - h_0)}, \tag{16}$$

where h_0 and P_0 represent the values of displacement and load at the actual point of contact, respectively. These values can be found by re-arranging Eq. 16 to yield a linear relationship between $P - \frac{2}{3}S_{\text{rep}}h_e$ and S_{rep}, with the slope equal to $-\frac{2}{3}h_0$ and the vertical intercept equal to P_0. Thus, the corrected load–displacement data are the reported data minus the values for P_0 and h_0. One major advantage of this approach is that no *a priori* knowledge of E_{eff} or R_{eff} is necessary. This approach is also suitable for anisotropic materials [3, 36]. However, this method does rely on accurate identification of the elastic-loading segment for fitting by linear regression, which is often a subjective procedure since, in practice, the transition between elastic and plastic deformation is not sharply defined [36, e.g., Fig. 4 in]. This difficulty in identifying the most appropriate segment of data for a linear fit introduces significant uncertainty in the calculated stress and strain [48].

In this section, we present an alternative formulation proposed by Breithaupt et al. [49], which is adapted from Kalidindi and Pathak [36] for the zero-point correction of load–displacement data. We calculate the values for P_0 and h_0 by minimizing the residual, r^*, between the data and predictions of perfect elasticity in the stress–strain curve. Thus, we define the residual, r, as [49]

$$r = \sigma - E_{\text{eff}}\varepsilon, \tag{17}$$

where the indentation stress, σ, and strain, ε, are defined according to Kalidindi and Pathak [36] and Pathak and Kalidindi [3] as follows:

$$\sigma = E_{\text{eff}}\varepsilon, \tag{18}$$

$$\sigma = \frac{P}{\pi a^2}, \tag{19}$$

$$\varepsilon = \frac{4h_e}{3\pi a}. \tag{20}$$

We can substitute these definitions for stress, strain, and contact radius in Eq. 17 and rearrange to yield

$$r = \frac{4E_{\text{eff}}^2}{3\pi}\left(\frac{3P - 2S_{\text{rep}}h_e}{S_{\text{rep}}^2}\right). \tag{21}$$

Recasting Eq. 21 in terms of reported and corrected values for load and displacement (similar to Eq. 16) and summing the absolute error lead to the proportionality [49]:

$$r_{\text{total}} \propto \sum \left|\left|\frac{3(P - P_0) - 2S_{\text{rep}}(h_e - h_0)}{S_{\text{rep}}^2}\right|\right|. \tag{22}$$

The residual in Eq. 22 describes the departure from elasticity. In practice, we find the values for h_0 and P_0 by minimizing r_{total}. We subtract the values for h_0 and P_0 from the uncorrected reported values to yield the corrected data for the point of zero contact. The advantage of this approach is that a significantly larger portion of the dataset is used than in the linear regression by Kalidindi and Pathak [36], and therefore, the correction is less sensitive to accurate identification of the elastic segment.

Calculation of Young's moduli

After the reported load–displacement data (P and h) are corrected for the effective point of contact by subtracting P_0 and h_0, respectively, we calculate the effective elastic modulus. In stiffer materials (e.g., olivine) with a clearly identifiable segment of elastic load–displacement, E_{eff} can be determined from Eq. 4, which requires the elastic displacement and effective radius to be known. However, any error in R_{eff} or in determining the elastic segment will significantly impact estimations of the effective Young's modulus. Importantly, if plastic yield occurs at shallow displacement, then the elastic displacement is not explicitly known and the sample curvature, R_s, becomes finite and modifies R_{eff} according to Eq. 6. This influence of plastic yielding is not easily accounted for and leads to an erroneous depth dependence of E_{eff}.

We can also use Eq. 10 to evaluate the Young modulus over the elastic segment, as previously done for reference materials in Fig. 5. However, Eq. 10 also relies on R_{eff} regardless of whether or not we use a constant radius or a load-dependent radius and is, therefore, subject to the same effects as the previous method if plastic yielding occurs.

Finally, we can calculate E_{eff} by assuming a constant radius and using Eqs. 14 and 15:

$$E_{\text{eff}} = \frac{\sqrt{\pi}}{2}\frac{S_{\text{corr}}}{\sqrt{2\pi R_i h_c - \pi h_c^2}}. \tag{23}$$

Because these equations are inherently based on the geometry of an ideal spherical tip, they are dependent on R_i and not on R_{eff}. Therefore, this method is not influenced by plastic yield of the surface [e.g., 31]. We implement Eq. 23 with corrected values for the harmonic stiffness measurement (Equation 9) and the contact depth (Equation 12), and use constant values for R_{eff} (Table A.1, column 1) to compute R_i. This approach is complementary to the one presented by Leitner et al. [31], who modify the parameters in Eq. 15 describing the geometry of the perfect tip for a given material. The advantage of our approach is that it inherently accounts for the effects of the machine stiffness. This approach is still applicable after plastic yield, which is particularly advantageous for materials with a short or noisy elastic segment. Moreover, any issues related to tip calibrations or machine-stiffness corrections will result in moduli that are

© The Author(s) 2023

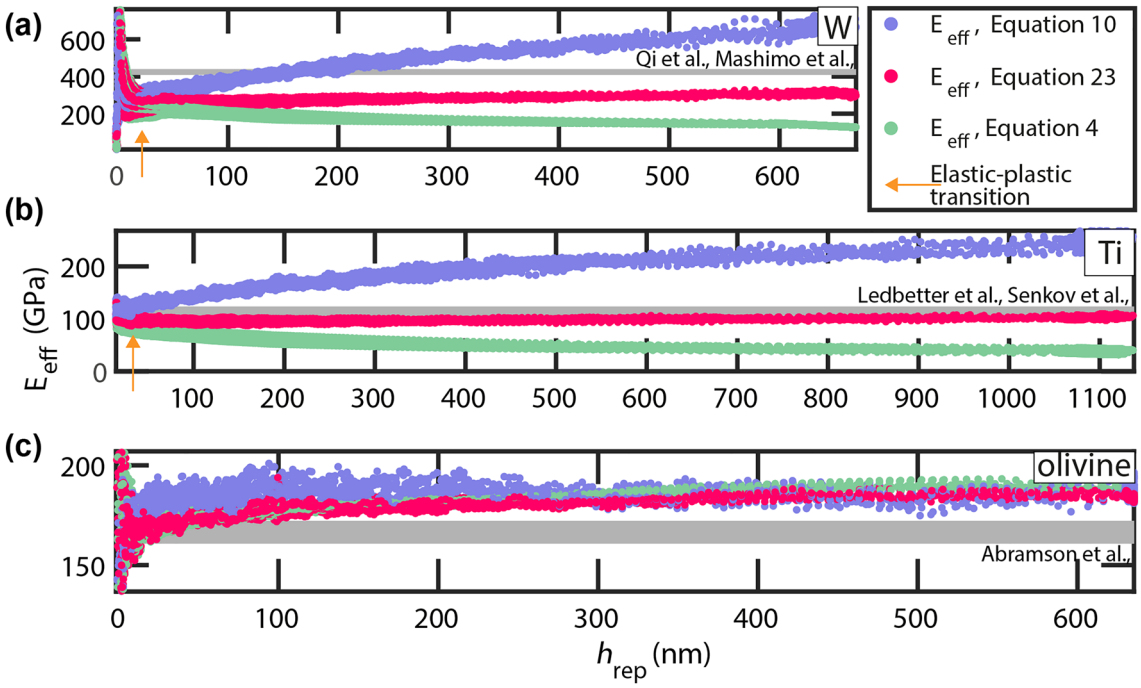

Figure 7: Measurements of Young's modulus for (a) tungsten (average E_{eff} = 306.7±14.2 GPa), (b) titanium (average E_{eff} = 99.5±4.7 GPa), and (c) olivine (average E_{eff} = 183.8±8.8 GPa) using data collected with a tip with a nominal radius of 50 µm. The grey horizontal lines indicate values obtained in previous studies on tungsten [50, 51], titanium [52, 53], and olivine [54]. The orange arrow indicates the approximate position of the elastic–plastic transition, which is absent in the fully elastic experiments on olivine. The effective Young's modulus is calculated using Eqs. 4 (green), 23 (red), and 10 (purple) to demonstrate that equations assuming elastic-only experiments diverge after the elastic–plastic transition.

not constant with indentation depth, flagging issues with the calibration.

Figure 7 displays examples of each these three approaches to measuring Young's modulus using tests in tungsten, titanium, and olivine conducted with a tip with a nominal radius of $R_n = 50\mu m$. As expected, the calculated moduli are comparable for elastic indentation at small displacements but diverge after plasticity initiates, at which point Eqs. 4 and 10 are no longer applicable. Moreover, Eq. 23 implemented with corrected values for h_c and R_i results in essentially constant values for Young's modulus, even after yield that are in agreement with previously published values for the tested materials [e.g., 3, 15].

Calculation of stress–strain curves and the yield point

Figure 8 presents stress–strain curves calculated for tungsten, titanium, and olivine using the spherical tips summarized in Table 1 and Eqs. 19 and 20 for stress and strain, respectively, as defined by Pathak and Kalidindi [3] and Kalidindi and Pathak [36]. All materials display an indentation size effect, in which the yield stress increases with decreasing effective radius. Note that the polycrystalline materials display a greater variability of stress values than the olivine single crystal due to plastic anisotropy [e.g., 48, 55]. Figure 8(a and b) displays E_{eff} values corresponding to averages of $E_s = 400 \pm 9$ GPa in W, and $E_s = 108 \pm 8$ GPa in Ti, which is in line with published values for W and on the lower end of the spectrum for Ti [3, 48, 55]. We calculate an indentation flow stress ranging between 4 and 10 GPa for W. In comparison, studies of indentation size effects using sharp tips document a hardness of 4 GPa in W at the greatest contact depths [e.g., 56, 57]. We calculate an indentation flow stress ranging between 1 and 3.5 GPa for Ti, in agreement with published spherical nanoindentation results in single crystals [48]. We note the absence of pop-ins in the indentation stress–strain curves collected in these polycrystalline samples, which is in contrast to the presence of pop-ins documented using spherical nanoindentation in both W [13] and Ti single crystals [48].

Furthermore, Fig. 7 highlights that the divergence of the moduli calculated with different formulations marks the yield point of the material. This result has a similar basis to the method proposed by Hackett et al. [14] for identifying the yield point. Their method, however, does not require *a priori* knowledge of R_{eff} or E_{eff}. To achieve this, Hackett et al. [14] compute the value S^3/P using two different methods for computing the contact stiffness. In the first method, the contact stiffness is obtained by differentiation [58] of the load–displacement curve, such that [14]

$$T_{slope} = \left(\frac{dP}{dh}\right)^3 P^{-1}. \quad (24)$$

© The Author(s) 2023

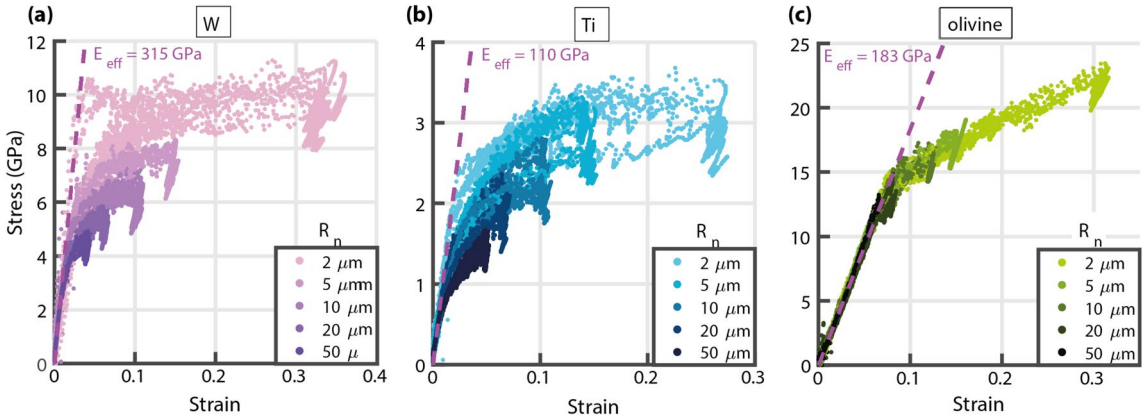

Figure 8: Summary of stress-strain curves in (a) tungsten, (b) titanium, and (c) olivine collected with spherical tips of varying radii. The dashed lines have the slope equal to the average E_{eff} across all indents. The displayed values of E_{eff} correspond to $E_s = 400 \pm 9$ GPa in tungsten, $E_s = 108 \pm 8$ GPa in titanium, and $E_s = 205 \pm 9$ GPa in olivine. The corresponding load-displacement curves are presented in Supplementary Materials (Fig. A.5).

This method calculating the stiffness is only valid for perfectly elastic portions of the loading curves. The second method uses the reported harmonic contact stiffness [14]:

$$T_{CSM} = \frac{S^3}{P}, \tag{25}$$

which is valid even if there is some plastic strain. These two estimates of S^3/P will be equivalent for elastic deformation and will diverge after plastic yield. Importantly, the first method relies on measurements of displacement and the second method relies on measurements of the harmonic contact stiffness, both of which will depend strongly on the corrections described in "Determination of machine stiffness" section.

In Fig. 9(a), we compute the elastic parameter S^3/P using both of these methods to identify the yield point for an indent in olivine collected using a tip with a nominal radius of 20 μm. We compare the yield point identified using reported values for S and h to the yield point identified using corrected values according to Eqs. 7 and 9. The light-colored data represent reported values, which are significantly different to the corrected data displayed in darker colors. The orange arrows and the blue-filled symbols mark the divergence point in the two independent calculations of the S^3/P parameter and the corresponding position of this point on the stress–strain curve for the same indent [insert in Fig. 9(a)]. Figure 9(a) highlights that this method is highly sensitive to the machine-stiffness corrections and the zero-point correction, with the point of divergence shifted by about 150 nm after applying the corrections.

In contrast to olivine, we are unable to distinguish an elastic segment implementing the method proposed by Hackett et al. [14] in titanium and tungsten with these

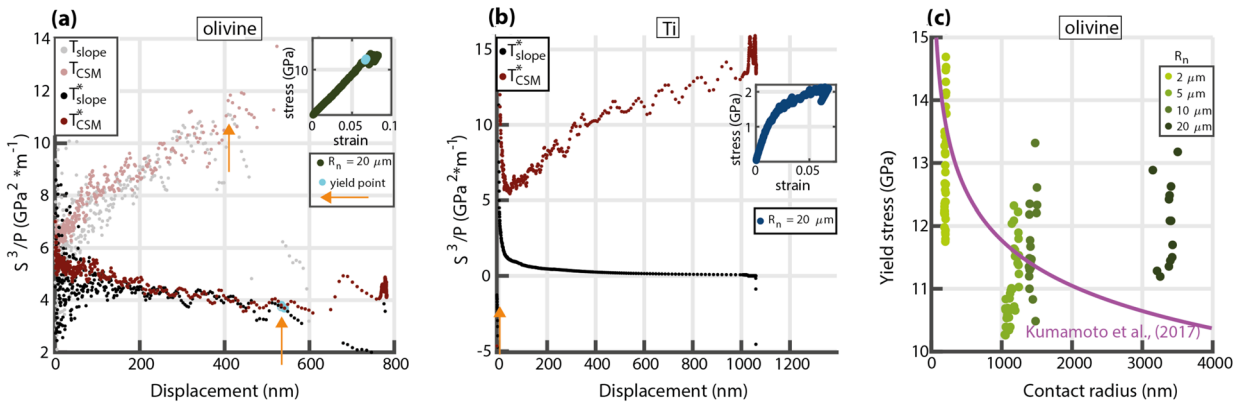

Figure 9: (a) Example calculations of S^3/P using Eqs. 24 and 25 proposed by Hackett et al. [14] using both reported (light colours, noted as T_{slope} and T_{CSM}) and corrected (dark colours, noted as T^*_{slope} and T^*_{CSM}) values. The corresponding stress-strain curve is presented in the insert. A filled-blue circle and an orange arrow mark the yield point on the corrected data in panel (a) and the insert. The data were collected with a tip with Rn = 20 μm. A smoothing window with an interval of 5 is applied to Tslope and T^*_{slope}. We present calculations for (a) olivine and (b) titanium. The elastic-plastic transition in panel (b) is indistinguishable as it occurs at small indentation depths. (c) Yield stress corresponding to the divergence point in panel (a) for olivine across tips with varying radii. The power law fit with an exponent of −0.09 has been determined by Kumamoto et al. [15] using spherical nanoindentation on similar samples, but deploying a different strategy for defining the yield stress.

© The Author(s) 2023

indentation contact sizes, as indicated by the immediately diverging values for E_{eff} at small depths in Fig. 7. For example, Fig. 9(b) displays the S^3/P parameter computed for Ti using data collected with a tip with a nominal radius of 20 μm, and corrected S and h values. The two calculations of the S^3/P parameter diverge at very small indentation depths (< 50 nm) consistent with the onset of plasticity at small displacements. Thus, this method is suitable only for materials displaying an elastic segment of minimum ≈ 100 nm [14]. Figure 9 emphasizes that, in ductile materials, the zero-point correction and determination of the Young's modulus following the methods proposed by Kalidindi and Pathak [36] and Pathak and Kalidindi [3] rely on data collected at small depths, which are heavily impacted by the quality of the initial contact.

To date, studies have implemented different conventions for determining the yield stress in spherical nanoindentation stress–strain curves [e.g., 9]. In this study, we picked the point of divergence exemplified in Fig. 9(a) for all indents in olivine and summarized the corresponding values in Fig. 9(c) as a function of their contact radii. Kumamoto et al. [15] used spherical nanoindentation and quantified a size effect in olivine in which the yield stress is proportional to the contact radius according to a power law with an exponent of −0.09. Figure 9(c) displays a size effect with some deviations from this power law. The discrepancy is likely due to the inherent differences in the definitions of the yield point, and possibly due to material anisotropy. Kumamoto et al. [15] present stress–strain curves in annealed single crystals with a pop-in associated with dislocation nucleation and glide after a longer segment of elastic loading compared to deformed samples. This phenomenon, documented in materials with scarce dislocation sources, is attributed to the requirement of a larger deformation volume for activating dislocation sources [e.g., 11, 12, 41]. The method presented in Fig. 9 implements a definition of the yield stress as the end of the elastic-loading segment [14]. However, in the indents displaying a pop-in, the point of divergence in Fig. 9(a) corresponds to stresses required for initiation of plasticity that are elevated relative to typical yield stresses because of the lack of dislocation sources. For example, Kumamoto et al [15] define yield stress as the intersection of the projected slope of the hardening curve at high strains with the elastic-loading curve, in line with other studies using spherical nanoindentation [e.g., 3]. Therefore, the apparent overestimate of the stresses in Fig. 9(c) for the largest contacts is consistent with the differences in the two conventions for the yield stress. Other studies implement a definition of the yield stress as the stress at a strain chosen by convention for a meaningful comparison with data obtained in uniaxial macroscale tests [e.g., 0.2% in 48, 59–62]. The calculated yield stress is a key outcome of spherical indentation and the choice of convention can influence the quantification of size effects in materials [e.g., 9].

Conclusions

We investigated in detail and further improved published methodologies for independently determining two key instrument parameters in spherical nanoindentation: system stiffness and effective radius of the indenter tip. To this end, we collect elastic data in reference materials with known moduli and highlight complexities in determining the effective radius using published protocols [e.g., 32]. We suggest a routine underpinned by parameterizing the effective radius as a function of load to overcome experimental errors. We benchmark our methodology against key criteria in spherical nanoindentation. We implement the tip calibrations on data collected on materials with unknown Young's modulus and varying ductility to calculate stress–strain curves. A summary diagram of this routine can be found in Supplementary Materials (Fig. A.4). These curves reveal a spherical indentation size effect in which the stress increases with indentation depth and with decreasing contact radius. We also test the influence of instrument parameters on published methods for determining the yield stress in materials with a significant elastic-loading segment [e.g., 14] and highlight the importance of consistency when establishing a convention for determining the yield stress. These improvements of the spherical nanoindentation technique are critical for refining the measurement and corrected values of the contact stiffness, given the importance of this measurement to the extraction of stress–strain curves, calculation of Young's modulus, and analysis of pop-ins [e.g., in Berkovich nanoindentation 43].

Experimental aspects

Nanoindentation tests with spherical tips and continuous stiffness measurements were performed with a load-controlled indenter (Nanoindenter G200, Agilent Technologies) with the frequency target set at 45 Hz, the harmonic displacement target set at 2 nm, and the loading rate divided by load set at $\frac{\dot{P}}{P} = 0.05\,\text{s}^{-1}$. We used diamond spherical tips ($E_i = 1141$ GPa, $\nu_i = 0.07$) with a 2–50 μm range of nominal tip radii (Table 1). The data collection was undertaken with the default machine stiffness, $S_{\text{default}} = 3.67 * 10^6$ N/m.

To assess tip calibration and data-analysis routines, we mounted reference materials with known moduli (fused silica, sapphire, and glassy carbon) on the same stub as materials with unknown elastic moduli (olivine, W, Ti) using the smallest amount of epoxy necessary. This set-up mediates differences in assembly stiffness due to the mounting substrate.

© The Author(s) 2023

The olivine single-crystal sample used in this study is the undeformed sample also used by Kumamoto et al. [sample MN1, 15, 63]. Both the titanium and tungsten samples are undeformed, commercially available pure samples, with grain sizes in the ranges of 10–50 μm and 10–100 μm, respectively.

We performed 270 nanoindentation tests in total, with at least 9 tests for each tip reported in Table 1. Nanoindentation experiments in materials with known Young's modulus were performed at small loads, resulting in elastic load–displacement curves (Table 1). We measured the harmonic contact stiffness throughout the loading and unloading paths in all experiments.

Acknowledgments

This work has been stimulated by conversations in the Oxford Micromechanics Group meetings. DA acknowledges useful conversations and input from Kathryn Kumamoto, David Armstrong, and Thomas Breithaupt.

Author contributions

We report authors' contributions according to CRediT taxonomy. Conceptualization: [AK], [DA], [LH]; Investigation: [AK], [DA]; Methodology: [DA], [LH]; Formal analysis and investigation: [DA]; Writing – original draft preparation: [DA]; Writing – review and editing: [AK], [LH], [AW]; Resources: [AKr], [AW]; Supervision: [LH], [AW];

Funding

DA is grateful to the UK National Environmental Research Council, and the Oxford Doctoral Training Partnership for DPhil studentship and funding from Grant NE/L002612/1. AK acknowledges support from the UK Engineering and Physical Research Council under Fellowship Grant EP/R030537/1. AJW and LH acknowledge support from the UK National Environmental Research Council under the Grant NE/S00162X/1.

Data availability

Nanoindentation data are available under an open access license, with the following DOI: https://doi.org/10.5281/zenodo.7607547.

Code availability

The authors will make the code available upon reasonable request.

Declarations

Conflict of interest On behalf of all authors, the corresponding author states that there is no conflict of interest.

Ethical approval

Not applicable.

Open Access

This article is licensed under a Creative Commons Attribution 4.0 International License, which permits use, sharing, adaptation, distribution and reproduction in any medium or format, as long as you give appropriate credit to the original author(s) and the source, provide a link to the Creative Commons licence, and indicate if changes were made. The images or other third party material in this article are included in the article's Creative Commons licence, unless indicated otherwise in a credit line to the material. If material is not included in the article's Creative Commons licence and your intended use is not permitted by statutory regulation or exceeds the permitted use, you will need to obtain permission directly from the copyright holder. To view a copy of this licence, visit http://creativecommons.org/licenses/by/4.0/.

Supplementary Information

The online version contains supplementary material available at https://doi.org/10.1557/s43578-023-01041-6.

References

1. A.C. Fischer-Cripps, Analysis of nanoindentation test data, in *Nanoindentation*. (Springer, 2011), pp.39–75
2. G.M. Pharr, E.G. Herbert, Y. Gao, The indentation size effect: a critical examination of experimental observations and mechanistic interpretations. Ann. Rev. Mater. Res. **40**, 271–292 (2010)
3. S. Pathak, S.R. Kalidindi, Spherical nanoindentation stress-strain curves. Mater. Sci. Eng.: R: Rep. **91**, 1–36 (2015). https://doi.org/10.1016/j.mser.2015.02.001
4. K. Johnson, The correlation of indentation experiments. J. Mech. Phys. Solids **18**(2), 115–126 (1970)
5. I. Spary, A. Bushby, N.M. Jennett, On the indentation size effect in spherical indentation. Phil. Mag. **86**(33–35), 5581–5593 (2006). https://doi.org/10.1080/14786430600854988
6. J.S. Weaver, S.R. Kalidindi, Mechanical characterization of ti-6al-4v titanium alloy at multiple length scales using spherical indentation stress-strain measurements. Mater. Design **111**, 463–472 (2016)
7. J. Swadener, E. George, G. Pharr, The correlation of the indentation size effect measured with indenters of various shapes. J. Mech. Phys. Solids **50**(4), 681–694 (2002). https://doi.org/10.1016/S0022-5096(01)00103-X
8. X. Hou, A. Bushby, N. Jennett, Study of the interaction between the indentation size effect and hall-petch effect with spherical

indenters on annealed polycrystalline copper. J. Phys. D: Appl. Phys. **41**(7), 074006 (2008)
9. E. Herbert, G. Pharr, W. Oliver, B. Lucas, J. Hay, On the measurement of stress-strain curves by spherical indentation. Thin Solid Films **398**, 331–335 (2001)
10. T. Zhu, A. Bushby, D. Dunstan, Size effect in the initiation of plasticity for ceramics in nanoindentation. J. Mech. Phys. Solids **56**(4), 1170–1185 (2008). https://doi.org/10.1016/j.jmps.2007.10.003
11. J.R. Morris, H. Bei, G.M. Pharr, E.P. George, Size effects and stochastic behavior of nanoindentation pop in. Phys. Rev. Lett. **106**(16), 165502 (2011). https://doi.org/10.1103/PhysRevLett.106.165502
12. S. Shim, H. Bei, E.P. George, G.M. Pharr, A different type of indentation size effect. Scripta Mater. **59**(10), 1095–1098 (2008)
13. H.D. Patel, S.-W. Lee, Spherical nanoindentation on tungsten single crystal: the transition from source-controlled plasticity to bulk plasticity. Scripta Mater. **175**, 16–19 (2020)
14. B. Hackett, A.A. Wereszczak, G. Pharr, Evaluation of new technique to estimate yield stress in brittle materials via spherical indentation testing, in *Proceeding of the 42nd International Conference on Advanced Ceramics and Composites: Ceramic Engineering and Science Proceedings*, vol. 39, 2nd edn. (John Wiley & Sons, Inc, Hoboken, NJ, USA, 2019), pp.61–71
15. K.M. Kumamoto, C.A. Thom, D. Wallis, L.N. Hansen, D.E. Armstrong, J.M. Warren, D.L. Goldsby, A.J. Wilkinson, Size effects resolve discrepancies in 40 years of work on low-temperature plasticity in olivine. Sci. Adv. **3**(9), e1701338 (2017). https://doi.org/10.1126/sciadv.1701338
16. L.N. Hansen, E.C. David, N. Brantut, D. Wallis, Insight into the microphysics of antigorite deformation from spherical nanoindentation. Phil. Trans. R. Soc. A **378**(2165), 20190197 (2020). https://doi.org/10.1098/rsta.2019.0197
17. S. Stich, K. Ding, Q.K. Muhammad, L. Porz, C. Minnert, W. Rheinheimer, K. Durst, J. Rödel, T. Frömling, X. Fang, Room-temperature dislocation plasticity in srtio3 tuned by defect chemistry. J. Am. Ceram. Soc. **105**(2), 1318–1329 (2022)
18. X. Fang, H. Bishara, K. Ding, H. Tsybenko, L. Porz, M. Höfling, E. Bruder, Y. Li, G. Dehm, K. Durst, Nanoindentation pop-in in oxides at room temperature: dislocation activation or crack formation? J. Am. Ceram. Soc. **104**(9), 4728–4741 (2021)
19. S.J. Vachhani, R.D. Doherty, S.R. Kalidindi, Studies of grain boundary regions in deformed polycrystalline aluminum using spherical nanoindentation. Int. J. Plasticity **81**, 87–101 (2016). https://doi.org/10.1016/j.ijplas.2016.01.001
20. J.S. Weaver, D.R. Jones, N. Li, N. Mara, S. Fensin, G.T. Gray III., Quantifying heterogeneous deformation in grain boundary regions on shock loaded tantalum using spherical and sharp tip nanoindentation. Mater. Sci. Eng. A **737**, 373–382 (2018). https://doi.org/10.1016/j.msea.2018.09.075
21. J. Li, G. Pharr, C. Kirchlechner, Quantitative insights into the dislocation source behavior of twin boundaries suggest a new dislocation source mechanism. J. Mater. Res. (2021). https://doi.org/10.1557/s43578-021-00253-y
22. A.J. Bushby, S.G. Roberts, C.D. Hardie, Nanoindentation investigation of ion-irradiated fe-cr alloys using spherical indenters. J. Mater. Res. **27**(1), 85–90 (2012). https://doi.org/10.1557/jmr.2011.304
23. D. Armstrong, C. Hardie, J. Gibson, A. Bushby, P. Edmondson, S. Roberts, Small-scale characterisation of irradiated nuclear materials: Part II nanoindentation and micro-cantilever testing of ion irradiated nuclear materials. J. Nucl. Mater. **462**, 374–381 (2015). https://doi.org/10.1016/j.jnucmat.2015.01.053
24. S. Pathak, S.R. Kalidindi, J.S. Weaver, Y. Wang, R.P. Doerner, N.A. Mara, Probing nanoscale damage gradients in ion-irradiated metals using spherical nanoindentation. Sci. Rep. **7**(1), 1–12 (2017). https://doi.org/10.1038/s41598-017-12071-6
25. S. Pathak, S.J. Vachhani, K.J. Jepsen, H.M. Goldman, S.R. Kalidindi, Assessment of lamellar level properties in mouse bone utilizing a novel spherical nanoindentation data analysis method. J. Mech. Behav. Biomed. Mater. **13**, 102–117 (2012). https://doi.org/10.1016/j.jmbbm.2012.03.018
26. L.H. He, N. Fujisawa, M.V. Swain, Elastic modulus and stress-strain response of human enamel by nano-indentation. Biomaterials **27**(24), 4388–4398 (2006). https://doi.org/10.1016/j.biomaterials.2006.03.045
27. I.-C. Choi, Y. Zhao, B.-G. Yoo, Y.-J. Kim, J.-Y. Suh, U. Ramamurty, J.-I. Jang, Estimation of the shear transformation zone size in a bulk metallic glass through statistical analysis of the first pop-in stresses during spherical nanoindentation. Scripta Mater. **66**(11), 923–926 (2012)
28. H. Bei, Z. Lu, E. George, Theoretical strength and the onset of plasticity in bulk metallic glasses investigated by nanoindentation with a spherical indenter. Phys. Rev. Lett. **93**(12), 125504 (2004)
29. T. Zhang, J. Ye, Y. Feng, Y. Ma, On the spherical nanoindentation creep of metallic glassy thin films at room temperature. Mater. Sci. Eng. A **685**, 294–299 (2017). https://doi.org/10.1016/j.msea.2017.01.018
30. D. Mercier, V. Mandrillon, G. Parry, M. Verdier, R. Estevez, Y. Bréchet, T. Maindron, Investigation of the fracture of very thin amorphous alumina film during spherical nanoindentation. Thin Solid Films **638**, 34–47 (2017). https://doi.org/10.1016/j.tsf.2017.07.040
31. A. Leitner, V. Maier-Kiener, D. Kiener, Essential refinements of spherical nanoindentation protocols for the reliable determination of mechanical flow curves. Mater. Design **146**, 69–80 (2018). https://doi.org/10.1016/j.matdes.2018.03.003
32. W. Li, H. Bei, J. Qu, Y. Gao, Effects of machine stiffness on the loading-displacement curve during spherical nano-indentation.

© The Author(s) 2023

J. Mater. Res. **28**(14), 2013 (1903). https://doi.org/10.1557/jmr.2013.164

33. A.J. Bushby, N.M. Jennett, Determining the area function of spherical indenters for nanoindentation. MRS Online Proc. Lib. **649**(1), 7171–7176 (2000). https://doi.org/10.1557/PROC-649-Q7.17
34. S.-K. Kang, Y.-C. Kim, Y.-H. Lee, J.-Y. Kim, D. Kwon, Determining effective radius and frame compliance in spherical nanoindentation. Mater. Sci. Eng. A **538**, 58–62 (2012). https://doi.org/10.1016/j.msea.2012.01.013
35. M. Cabibbo, P. Ricci, R. Cecchini, Z. Rymuza, J. Sullivan, S. Dub, S. Cohen, An international round-robin calibration protocol for nanoindentation measurements. Micron **43**(2–3), 215–222 (2012). https://doi.org/10.1016/j.micron.2011.07.016
36. S.R. Kalidindi, S. Pathak, Determination of the effective zero-point and the extraction of spherical nanoindentation stress-strain curves. Acta Mater. **56**(14), 3523–3532 (2008). https://doi.org/10.1016/j.actamat.2008.03.036
37. X. Li, B. Bhushan, A review of nanoindentation continuous stiffness measurement technique and its applications. Mater. Characterization **48**(1), 11–36 (2002). https://doi.org/10.1016/S1044-5803(02)00192-4
38. W.C. Oliver, G.M. Pharr, An improved technique for determining hardness and elastic modulus using load and displacement sensing indentation experiments. J. Mater. Res. **7**(6), 1564–1583 (1992). https://doi.org/10.1557/JMR.1992.1564
39. J. G. Swadener and G. M. Pharr. A methodology for the calibration of spherical indenters. MRS Online Proc. Lib. (OPL), 594 (1999)
40. J. Field, M. Swain, A simple predictive model for spherical indentation. J. Mater. Res. **8**(2), 297–306 (1993). https://doi.org/10.1557/JMR.1993.0297
41. H. Bei, Y. Xia, R.I. Barabash, Y. Gao, A tale of two mechanisms: strain-softening versus strain-hardening in single crystals under small stressed volumes. Scripta Mater. **110**, 48–52 (2016)
42. Y. Gao, H. Bei, Strength statistics of single crystals and metallic glasses under small stressed volumes. Progress Mater. Sci. **82**, 118–150 (2016)
43. P. SudharshanPhani, W. Oliver, G. Pharr, Measurement of hardness and elastic modulus by load and depth sensing indentation: improvements to the technique based on continuous stiffness measurement. J. Mater. Res. **36**(11), 2137–2153 (2021)
44. B. Merle, V. Maier, M. Göken, K. Durst, Experimental determination of the effective indenter shape and ε-factor for nanoindentation by continuously measuring the unloading stiffness. J. Mater. Res. **27**(1), 214–221 (2012)
45. I.N. Sneddon, The relation between load and penetration in the axisymmetric boussinesq problem for a punch of arbitrary profile. Int. J. Eng. Sci. **3**(1), 47–57 (1965). https://doi.org/10.1016/0020-7225(65)90019-4
46. S. Basu, A. Moseson, M.W. Barsoum, On the determination of spherical nanoindentation stress-strain curves. J. Mater. Res. **21**(10), 2628–2637 (2006)
47. A.J. Moseson, S. Basu, M.W. Barsoum, Determination of the effective zero point of contact for spherical nanoindentation. J. Mater. Res. **23**(1), 204–209 (2008)
48. J.S. Weaver, M.W. Priddy, D.L. McDowell, S.R. Kalidindi, On capturing the grain-scale elastic and plastic anisotropy of alpha-ti with spherical nanoindentation and electron back-scattered diffraction. Acta Mater. **117**, 23–34 (2016)
49. T. Breithaupt, L. Hansen, D. Wallis, D. Armstrong. Low-temperature plasticity of plagioclase from indentation. Master's thesis (University of Oxford, 2017)
50. X. Qi, N. Cai, T. Chen, S. Wang, B. Li, Experimental and theoretical studies on the elasticity of tungsten to 13 gpa. J. Appl. Phys. **124**(7), (2018)
51. T. Mashimo, X. Liu, M. Kodama, E. Zaretsky, M. Katayama, K. Nagayama, Effect of shear strength on hugoniot-compression curve and the equation of state of tungsten (w). J. Appl. Phys. **119**(3), (2016)
52. H. Ledbetter, H. Ogi, S. Kai, S. Kim, M. Hirao, Elastic constants of bodycentered cubictitanium monocrystals. J. Appl. Phys. **95**(9), 4642–4644 (2004)
53. O. Senkov, M. Dubois, J. Jonas, Elastic moduli of titanium-hydrogen alloys in the temperature range 20 °C to 1100 °C. Metall. Mater. Trans. A **27**, 3963–3970 (1996)
54. E. Abramson, J. Brown, L. Slutsky, J. Zaug, The elastic constants of san carlos olivine to 17 gpa. J. Geophys. Res. Solid Earth **102**(B6), 12253–12263 (1997)
55. T. Britton, H. Liang, F. Dunne, A. Wilkinson, The effect of crystal orientation on the indentation response of commercially pure titanium: experiments and simulations. Proc. R. Soc. A: Math. Phys. Eng. Sci. **466**(2115), 695–719 (2010)
56. F. Javaid, Y. Xu, E. Bruder, K. Durst, Indentation size effect in tungsten: quantification of geometrically necessary dislocations underneath the indentations using hr-ebsd. Mater. Characterization **142**, 39–42 (2018)
57. V. Maier, C. Schunk, M. Göken, K. Durst, Microstructure-dependent deformation behaviour of bcc-metals-indentation size effect and strain rate sensitivity. Phil. Mag. **95**(16–18), 1766–1779 (2015)
58. D. Rowland. diffxy.https://www.mathworks.com/matlabcentral/fileexchange/29312-diffxy
59. D.K. Patel, S.R. Kalidindi, Correlation of spherical nanoindentation stress-strain curves to simple compression stress-strain curves for elastic-plastic isotropic materials using finite element models. Acta Mater. **112**, 295–302 (2016)
60. A. Iskakov, S.R. Kalidindi, Multiresolution investigations of thermally aged steels using spherical indentation stress-strain protocols and image analysis. Mech. Mater. **167**, 104265 (2022)

© The Author(s) 2023

61. Z.S. Courtright, N.P. Leclerc, H.N. Kim, S.R. Kalidindi, Critical comparison of spherical microindentation, small punch test, and uniaxial tensile testing for selective laser melted inconel 718. Appl. Sci. **11**(3), 1061 (2021)
62. A. Khosravani, L. Morsdorf, C.C. Tasan, S.R. Kalidindi, Multiresolution mechanical characterization of hierarchical materials: spherical nanoindentation on martensitic fe-ni-c steels. Acta Mater. **153**, 257–269 (2018)
63. D. Wallis, L.N. Hansen, K.M. Kumamoto, C.A. Thom, O. Plümper, M. Ohl, W.B. Durham, D.L. Goldsby, D.E. Armstrong, C.D. Meyers et al., Dislocation interactions during low-temperature plasticity of olivine and their impact on the evolution of lithospheric strength. Earth Planet. Sci. Lett. **543**, 116349 (2020)

Publisher's Note Springer Nature remains neutral with regard to jurisdictional claims in published maps and institutional affiliations.

© The Author(s) 2023